High resolution imaging of embryonic mouse samples with a laser-driven betatron x-ray source

Contact: j.cole11@imperial.ac.uk

J. M. Cole, K. Poder, N. C. Lopes, J. C. Wood, S. Alatabi, C. Kamperidis, S. P. D. Mangles, Z. Najmudin
The John Adams Institute for Accelerator Science Imperial College London, London, SW7 2AZ, UK

D. Norris, J. Sanderson, L. Teboul, H. Westerberg, M. Sandholzer, S. Johnson, Z. Szoke-Kovacs
Mammalian Genetics Unit, MRC Harwell Harwell Campus, UK

M. A. Hill, M. De Lazzari, J. Thomson
CRUK/MRC Oxford Institute for Radiation Oncology University of Oxford, Oxford, UK

D. R. Symes, D. Rusby, P. S. Foster, S. Botchway, S. Gratton
Central Laser Facility, STFC Rutherford Appleton Laboratory, Chilton, Didcot, OX11 0QX, UK

C. A. J. Palmer, O. Kononenko
Deutsches Elektronen-Synchrotron Notkestrasse 85, 22607 Hamburg, Germany

J. R. Warwick, G. Sarri
Centre for Plasma Physics, Queens University Belfast Belfast, BT7 1NN, UK

Abstract

An imaging beamline was constructed around a laser-driven betatron x-ray source at the Gemini laser facility, and operated at a significantly higher average photon flux than previously possible. The x-ray source was energetically stable to within $\pm 6\%$ over hundreds of laser shots, and facilitated the acquisition of 2D radiographs of embryonic mouse samples on a single shot basis, at high resolution and signal-to-noise ratio.

1 Introduction

Laser wakefield accelerators are an emerging class of compact particle accelerators driven by high-intensity lasers [1, 2], capable of the acceleration of electron beams up to the GeV level over several centimetres [3, 4, 5]. The longitudinal accelerating field is created by separating charged species in a plasma, generating electric fields up to several 100s GeV/m. As the electrons bunch is accelerated longitudinally, it experiences transverse focussing electromagnetic forces from the plasma which convert any transverse momentum into a transverse oscillation. This oscillation causes the electron bunch to radiate, at photon energies boosted by the high average Lorentz factor of the electron bunch to the hard x-ray range. Such 'betatron' radiation has been shown to be bright, ultrashort, and originate from a spatial volume of micron-scale transverse size [6, 7].

These features make betatron x-ray sources attractive for imaging purposes where, for point-projection radiography, the maximum spatial resolution of the image is proportional to the size of the x-ray source. Previous work in this field has examined the imaging quality of betatron backlighters with insect [8, 9] and human bone [10] samples.

In this Report an experiment is described where a betatron x-ray source was used to image embryonic mouse samples, whose categorisation is important in the context of the International Mouse Phenotyping Consortium [11]. In comparison to previous work, the mean peak brightness of the x-ray source was larger by a factor of > 10 [12], producing radiographs with significantly higher signal-to-noise ratio (SNR) than previously achieved. Proof-of-principle biomedical imaging results of this kind will pave the way towards the deployment of compact laser-driven betatron sources operating at a significantly higher average flux and shorter exposure time than any other laboratory-scale x-ray source.

2 Beamline

The experiment took place in 2015 at the Gemini laser facility, RAL, UK. One of the Gemini beams was used to drive a laser wakefield as part of the x-ray beamline - see Fig. 1.

The wakefield driver beam was focussed with an $f/40$ spherical mirror to a FWHM spot size of $(40 \pm 1) \times (52 \pm 4)$ µm, and delivered 10.4 ± 0.5 J to the target. After correction with a large-aperture adaptive optic, the FWHM contour of the focal spot contained a fraction $\alpha = 0.33 \pm 0.02$ of the pulse energy. The pulse length for the imaging shots was $\tau_{\text{FWHM}} = 51 \pm 5$ fs, reaching a peak intensity of $(6.3 \pm 0.6) \times 10^{18}\,\text{Wcm}^{-2}$, or peak $a_0 = 1.71 \pm 0.09$

The plasma was confined to a helium gas cell of variable length. The plasma channel spatial profile and density was recorded on each shot with transverse shadowgraphy and moiré deflectometry, using the second arm of Gemini as an ultrafast probe. The plasma density and

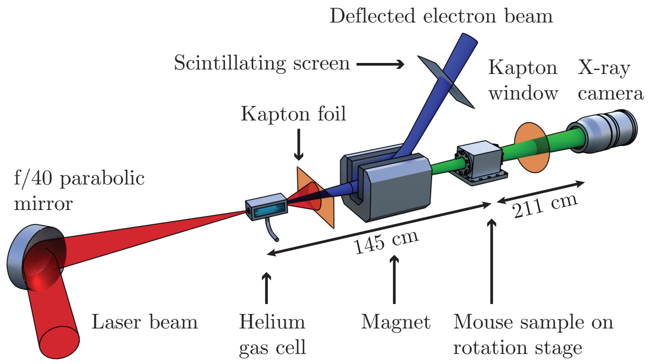

Figure 1: The x-ray beamline layout inside the main Gemini vacuum chamber. One of the Gemini beams (red) is focussed into a helium gas cell, producing co-propagating electron (blue) and x-ray (green) beams.

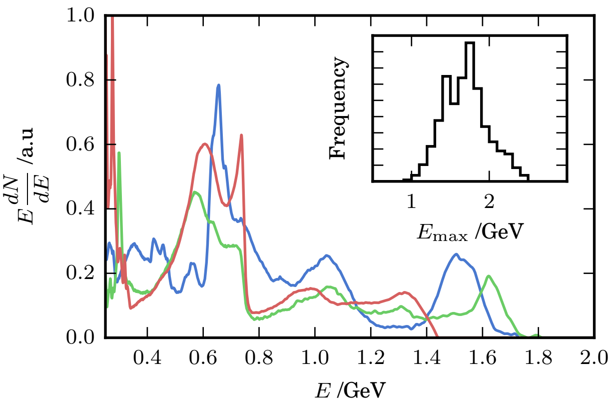

Figure 2: Typical electron spectra as recorded during the imaging shots, consisting of high-charge, $\sim$ 0.7 GeV and low-charge, $\sim$ 1.5 GeV components. *Inset* - histogram of peak electron energies during imaging shots.

length was varied as so to optimise the stability and flux of the betatron beams. For the images presented here, the plasma length was 20 mm and the electron density was $(2.6 \pm 0.3) \times 10^{18}\,\mathrm{cm}^{-3}$.

To prevent any damage to the imaging samples, the laser pulse was first blocked with a reflector foil, consisting of a 25 µm layer of Kapton, flash-coated with a thin layer of aluminium. To minimise bremsstrahlung noise, the electron beam was deflected upwards by a series of permanent dipole magnets with a total magnetic length of $\int B(x)\,\mathrm{d}x = 0.4\,\mathrm{Tm}$. The magnetically dispersed electron beam was recorded on a pair of scintillating Gd_2O_2S:Tb screens, each imaged with a cooled 16-bit CCD camera. The electron spectrum and average angular offset from the laser axis were simultaneously retrieved from the multiple scintillator images [13].

The imaging samples were mounted on a compact rotation stage inside a sealed sample chamber, maintained at atmospheric pressure inside the main vacuum chamber. A degree of thermal control was available through an attached heatsink and Peltier cooler. The windows of the sample chamber consisted of a pair of 50 µm Kapton foils, with an additional protective layer of 24 µm aluminium on the front of the chamber.

The vacuum chamber was sealed on the beamline axis with a 250 µm thick Kapton window, and the x-ray beam propagated 48 cm in air before reaching the x-ray detector. For the images discussed here, the detector was a 150 µm thick structured CsI scintillator fibre-coupled to a 2048×2048 pixel CCD camera. The pixel size was 13.5×13.5 µm for a detector area of 27.7×27.7 mm and angular acceptance of 7.8 mrad.

3 Beam properties

As plotted in Fig. 2 the electron spectra for these plasma conditions were broad, typically consisting of a high-charge, low-energy component and a low-charge, high-energy component. The charge in the low-energy component was observed to be correlated with the betatron x-ray flux [12], so it is likely this component was responsible for the bulk of the photon emission. The peak energies of the beams were high compared to shorter focal length configurations of the Gemini system, often exceeding 2 GeV [13].

The x-ray flux was also significantly increased compared to previous experiments, reaching $\approx 3 \times 10^{10}$ photons above 1 keV per laser shot. The FWHM beam area overfilled the detector, and the FWHM divergence was approximately 10 mrad in each direction. Coupled with a laser repetition rate of 0.05 Hz, the average photon flux above 1 keV was $\approx 9 \times 10^6$ ph/s/mrad^2. This average flux is a factor of 10-100 higher than that possible with a conventional laboratory-scale x-ray source of micron size [14], and ensures that one radiographic exposure requires only one laser shot.

By calculating the relative opacity of the elemental filters (visible in Fig. 4) and assuming an on-axis synchrotron spectrum for the x-ray beam, a best-fit spectrum was found for each shot. Such a spectrum is characterised by a critical energy E_{crit}, which is near the modal energy of the broadband spectrum. For these plasma conditions the energies were remarkably constant at $E_{\mathrm{crit}} = 18 \pm 1$ keV over > 300 shots. It should be noted that this is the energy as measured towards the edges of the beam. As the imaging sample occupies the brightest central portion, and betatron beams are measured to become softer at larger radius [15], this measurement is therefore likely an underestimate of the E_{crit} at the centre of the beam, which if up to 40% higher [16] could be near $E_{\mathrm{crit}} \approx 25\,\mathrm{keV}$.

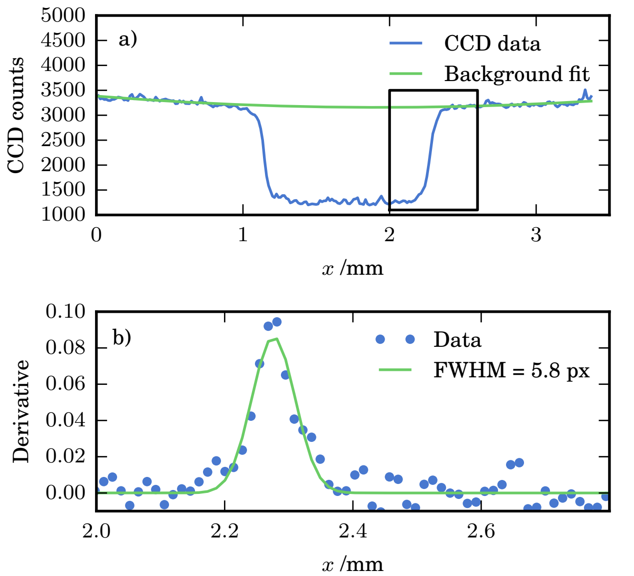

Figure 3: a) Averaged lineout through most opaque filter element, and fitted 2nd-order polynomial background. b) Derivative of ESF highlighted in a), with best-fit Gaussian overlaid.

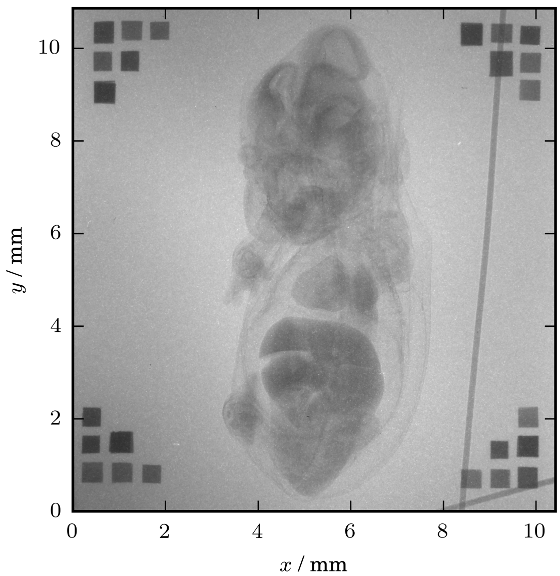

Figure 4: An exemplary radiograph of the mouse sample. The axes refer to spatial dimensions at the object plane. The squares in each corner are elemental filters for the on-shot transmission spectroscopy, and the thin wires act as fiducials to account for the source motion.

4 Imaging results

The mouse sample was a 14.5 day embryo of height 10.2 ± 0.1 mm stained with iodine potassium iodide and suspended in agarose. The stain acted as an absoprtion contrast enhancement agent, composed of high-Z elements which are more opaque to > 10 keV x-ray photons than soft tissue. The stain is absorbed at different rates in different organs, leading to differential photon absorption and generating additional radiographic contrast. When installed inside the sample chamber the source-sample distance was 1451 mm and the sample-camera distance was 2110 mm for a geometric magnification of $M = 2.46$. As plotted in Fig. 3, the spatial resolution of the scintillator was estimated from the edge-spread-function (ESF) of one of the metal filters in the corner of the image. By fitting a smooth background behind the filter to eliminate the non-uniformity in the x-ray beam profile, the (assumed isotropic) point-spread-function (PSF) is estimated by fitting a Gaussian to the spatial derivative of the ESF. In this manner, the FWHM of the PSF was estimated to be 5.8 pixels, corresponding to 78 µm at the detector or 32 µm at the sample plane. This is significantly larger than the x-ray source size, and so is the limiting factor on achievable spatial resolution here.

An example radiograph is displayed in Fig. 4, where the detector nonuniformities have been subtracted and hot pixels removed with a 3×3 median filter. The image has not been corrected for x-ray beam inhomogeneity, and so is indicative of the spatial profile of the x-ray beam during the experiment.

Clearly visible are the major contrast-stain absorbing organs such as the liver, kidneys, and heart. The minimum transmission of the sample is above 50%, indicating that the x-ray energy is appropriate for such a relatively opaque sample. Importantly, fine features such as the skin, whisker buds, and ribcage are also rendered with clarity, and remain well resolved across the image.

An important quantity to measure and optimise in radiography is the signal-to-noise ratio (SNR) of the image, defined as the local ratio of the smooth backlighter signal to the random noise present. The local SNR of the radiograph in Fig. 4 is plotted in Fig. 5, typically reaching up to ≈ 20 throughout the region of the image containing the mouse sample.

If the noise is assumed to arise from Poisson photon noise, and it is assumed that each pixel receives ≈ 2000 photons per pixel per shot, the source-limited SNR is approximately $2000/\sqrt{2000} \approx 44$. Additional sources of noise include the photon conversion process in the scintillator (due to a compounding of Poisson effects) and bremsstrahlung photons from the electron beam. The peak measured SNR outside the sample is therefore reasonably near the physical limit given the available flux, and that inside the sample is more than sufficient for most radiographic purposes. A lower bound on SNR of 2-4 for feature detectability in radiography has been measured [17, 18, 19], though in general the SNR required for the perception threshold scales as

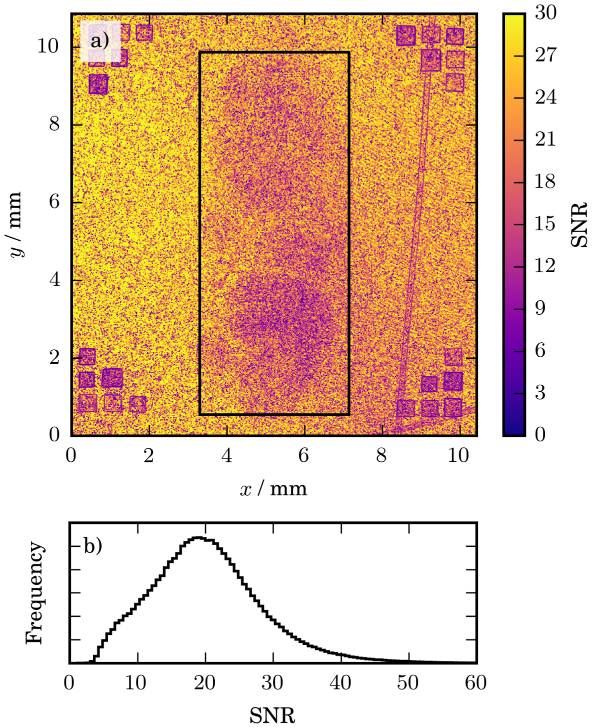

Figure 5: a) SNR as calculated for each pixel in Fig. 4 over a local 5 × 5 pixel window. b) Histogram of SNR over the region highlighted in a).

$$\text{SNR threshold} \approx 10 \times \frac{\text{PSF FWHM}}{\text{Feature size}}$$

where the factor of 10 is determined empirically. A peak SNR of greater than 10 then implies feature detectability down to the limit set by the detector resolution.

5 Conclusion

High quality radiography of a complex and significantly opaque embryonic mouse sample was achieved on a single-shot basis at very high average photon flux. The x-ray beam profile was homogenous enough to illuminate the entire sample uniformly, and the beam energy remained constant to within $\pm 6\%$ over hundreds of exposures. This achievement is a significant step towards high-throughput radiography and tomography of small-animal samples for preclinical imaging on laser-driven betatron sources.

Acknowledgements

We would like to acknowledge the support of CLF staff in the running of this experiment. We acknowledge funding from STFC for the support of the John Adams Institute of Accelerator Science by grants ST/J002062/1 and ST/P000835/1.

References

[1] S. P. D. Mangles et al. Monoenergetic beams of relativistic electrons from intense laser-plasma interactions. *Nature* **431,** 7008 (2004), pp. 535–538.

[2] E. Esarey, C. B. Schroeder, and W. P. Leemans. Physics of laser-driven plasma-based electron accelerators. *Reviews of Modern Physics* **81,** 3 (2009), pp. 1229–1285.

[3] H. T. Kim et al. Enhancement of electron energy to the multi-gev regime by a dual-stage laser-wakefield accelerator pumped by petawatt laser pulses. *Physical Review Letters* **111,** 16 (2013), pp. 1–5. arXiv:1307.4159.

[4] X. Wang et al. Quasi-monoenergetic laser-plasma acceleration of electrons to 2 GeV. *Nature Communications* **4,** May (2013).

[5] W. P. Leemans et al. Multi-GeV Electron Beams from Capillary-Discharge-Guided Subpetawatt Laser Pulses in the Self-Trapping Regime. *Physical Review Letters* **113,** (2014), p. 245002.

[6] A. Rousse et al. Production of a keV x-ray beam from synchrotron radiation in relativistic laser-plasma interaction. *Physical Review Letters* **93,** 13 (2004), p. 135005.

[7] S. Kneip et al. Bright spatially coherent synchrotron X-rays from a table-top source. *Nature Physics* **6,** 12 (2010), pp. 980–983.

[8] S. Kneip et al. X-ray phase contrast imaging of biological specimens with femtosecond pulses of betatron radiation from a compact laser plasma wakefield accelerator. *Applied Physics Letters* **99,** 9 (2011), p. 093701.

[9] J. Wenz et al. Quantitative X-ray phase-contrast microtomography from a compact laser-driven betatron source. *Nature Communications* **6,** (2015), p. 7568.

[10] J. M. Cole et al. Laser-wakefield accelerators as hard x-ray sources for 3D medical imaging of human bone. *Scientific Reports* **5,** (2015), p. 13244.

[11] S. D. M. Brown and M. W. Moore. The International Mouse Phenotyping Consortium: past and future perspectives on mouse phenotyping. *Mammalian Genome* **23,** 9-10 (2012), pp. 632–640. arXiv:NIHMS150003.

[12] J. C. Wood et al. Enhanced Betatron Radiation from a Laser Wakefield Accelerator in a Long Focal Length Geometry. *CLF Annual Report* (2017).

[13] K. Poder et al. Multi-GeV electron acceleration in strongly non-linear wakefield driven by oversized laser spots. *In preparation* (2017).

[14] B Verman, L Jiang, and B Kim. Microfocusing source and multilayer optics based x-ray diffraction systems. *The Rigaku Journal* **19,** 1 (2002), pp. 4–13.

[15] F. Albert et al. Angular Dependence of Betatron X-Ray Spectra from a Laser-Wakefield Accelerator. *Physical Review Letters* **111,** 23 (2013), p. 235004.

[16] J. C. Wood. Betatron Radiation from Laser Wakefield Accelerators and its Applications. PhD Thesis. Imperial College London, 2016.

[17] R. Aufrichtig and P. Xue. Dose efficiency and low-contrast detectability of an amorphous silicon x-ray detector for digital radiography. *Physics in Medicine and Biology* **45,** 9 (2000), pp. 2653–2669.

[18] M. Ishida et al. Digital image processing: effect on detectability of simulated low-contrast radiographic patterns. *Radiology* **150,** 2 (1984), pp. 569–575.

[19] K. Ohara et al. Investigation of basic imaging properties in digital radiography. 8. Detection of simulated low-contrast objects in digital subtraction angiographic images. *Medical Physics* **13,** 3 (1986), pp. 304–311.